

## RESEARCH ARTICLE

# Ultrafast Martensitic Phase Transition Driven by Intense Terahertz Pulses

B. Q. Song<sup>1,2†</sup>, X. Yang<sup>1,2†</sup>, C. Sundahl<sup>3</sup>, J.-H. Kang<sup>3</sup>, M. Mootz<sup>1,4</sup>, Y. Yao<sup>2</sup>, I. E. Perakis<sup>4</sup>, L. Luo<sup>2</sup>, C. B. Eom<sup>3</sup>, and J. Wang<sup>1,2\*</sup>

<sup>1</sup>Department of Physics and Astronomy, Iowa State University, Ames, IA 50011, USA. <sup>2</sup>Ames National Laboratory of U.S. DOE, Ames, IA 50011, USA. <sup>3</sup>Department of Materials Science and Engineering, University of Wisconsin-Madison, Madison, WI 53706, USA. <sup>4</sup>Department of Physics, University of Alabama at Birmingham, Birmingham, AL 35294-1170, USA.

\*Address correspondence to: [jgwang@ameslab.gov](mailto:jgwang@ameslab.gov)

†These authors contributed equally to this work.

We report on an ultrafast nonequilibrium phase transition with a strikingly long-lived martensitic anomaly driven by above-threshold single-cycle terahertz pulses with a peak field of more than 1 MV/cm. A nonthermal, terahertz-induced depletion of low-frequency conductivity in Nb<sub>3</sub>Sn indicates increased gap splitting of high-energy  $\Gamma_{12}$  bands by removal of their degeneracies, which induces the martensitic phase above their equilibrium transition temperature. In contrast, optical pumping leads to a  $\Gamma_{12}$  gap thermal melting. Such light-induced nonequilibrium martensitic phase exhibits a substantially enhanced critical temperature up to  $\sim 100$  K, i.e., more than twice the equilibrium temperature, and can be stabilized beyond technologically relevant, nanosecond time scales. Together with first-principle simulations, we identify a compelling terahertz tuning mechanism of structural order via  $\Gamma_{12}$  phonons to achieve the ultrafast phase transition to a metastable electronic state out of equilibrium at high temperatures far exceeding those for equilibrium states.

## Introduction

An emerging paradigm for condensed matter physics is ultrafast light-induced correlation phenomena and phase transitions in, e.g., superconductivity [1–5], density wave collective orders [6], magnetism [7–9], and time-evolving topological transition [10–12]. These developments reflect an evolving nature for understanding the concept “phase.” That is, a phase can be interpreted as a finite lifetime fashion, referred to as metastable states that live in a post-quench prethermalization time scale of picoseconds to nanoseconds [13]. Correspondingly, the phase diagram is extended to the time domain, where many metastable orders are discovered [1,14]. Of particular interest are the strongly correlated electronic systems [2,15] in which emergent orders might coexist and display an intertwined behavior [16].

It remains a challenge to develop efficient, nonthermal tuning knobs at terahertz clock rates and to stabilize transient photoinduced phases at many nanosecond time scales. In contrast to high-energy optical excitation, the advent of intense single- and few-cycle terahertz pulses with a peak field of more than 1,000 kV/cm represents a unique opportunity for phase switching and stabilization by applying a lightwave dynamic symmetry breaking principle [17] with minimum heating of electronic states [13,18,19]. A compelling example is the possibility to achieve light-induced superconductivity via multi-terahertz nonlinear structural pumping in cuprates, which persists far

above equilibrium critical temperatures although it lasts only for a few picoseconds [2]. Unlike in these intensely debated, complex materials, A<sub>3</sub>B compounds, such as Nb<sub>3</sub>Sn with A15 crystal structure, represent simpler and well-understood model-correlated materials [13,20], which are well suited for seeking examples of nonequilibrium phase transition by using phonon pumping. Such terahertz lattice driving is still scarce, despite recent progress [2,11,12,14,18,21,22]. Here, we use Nb<sub>3</sub>Sn to address 2 outstanding general issues: (a) Can intense terahertz light pump fields create long-lived martensitic orders far above equilibrium critical temperatures? (b) What are the salient features of the nonthermal tuning of structural fluctuations that give rise to such controllable nonequilibrium order?

## Materials and Methods

The structure of Nb<sub>3</sub>Sn (Fig. 1A) is cubic (*Pm3n*) at higher temperature and undergoes martensitic transition (MT) to tetragonal (*P4<sub>2</sub>/mmc*) at  $T_M \sim 47$  K. An alternative view to regard MT is “dimerization” of Nb atoms that were originally equally spaced along the chains (blue dash lines in Fig. 1A) [23]. One can understand such an MT behavior as optical phonon condensation [23–26]. Once a symmetry breaking phonon occurs, along *z* axis, the next-coming phonons will follow the same pathway, with less chance to enter other modes along *x* or *y* axis, eventually causing a permanent distortion. This picture is vital for understanding the dynamic MT, which is

**Citation:** Song BQ, Yang X, Sundahl C, Kang JH, Mootz M, Yao Y, Perakis IE, Luo L, Eom CB, Wang J. Ultrafast Martensitic Phase Transition Driven by Intense Terahertz Pulses. *Ultrafast Sci.* 2023;3:Article 0007. <https://doi.org/10.34133/ultrafastscience.0007>

Submitted 2 August 2022  
Accepted 1 December 2022  
Published 16 January 2023

Copyright © 2023 B. Q. Song et al. Exclusive Licensee Xi'an Institute of Optics and Precision Mechanics. No claim to original U.S. Government Works. Distributed under a Creative Commons Attribution License (CC BY 4.0).

temporally induced by laser and lasts for  $t_L$  of nanosecond time scales. Meanwhile, the photon energy will transfer into phonon vibration along a specific direction, rather than equipartition; beyond  $t_L$ , however, the inequity of energy along different axes elapses and symmetry recovers (Fig. 1A). Such structural (cubic tetragonal) and phonon softening anomalies can originate from twofold degenerate  $\Gamma_{12}$  subbands crossing the Fermi level (FL), with density of states (DOS) that determines  $T_M$  of the MT phase. Therefore, the  $\Gamma_{12}$  phonon pumping by an intense, few-cycle terahertz-pulse of  $\sim 1,000$  kV/cm, without the substantial heating of other degrees of freedom, provides a compelling avenue to induce a nonequilibrium martensitic phase at temperatures far exceeding the equilibrium  $T_M$  by lifting the electronic degeneracy and increasing DOS of the  $\Gamma_{12}$  bands. Although quantum quench of superconducting (SC) states has been actively explored in  $\text{Nb}_3\text{Sn}$  [13], the terahertz-driven martensitic normal states have never been explored, which is different compared with its static counterpart [27]. The dynamic martensitic order parameter  $\phi$  usually exhibits  $T_M^* \neq T_M$ . Moreover, static MT is reflected by phonon softening anomalies [23,27]; for dynamic MT,  $\phi$  will be detected by the change of single-cycle electric field  $\Delta E_{\text{THz}}$ , which is measured at ultrafast time scales and, thus, depends on an “instantaneous” order parameter.

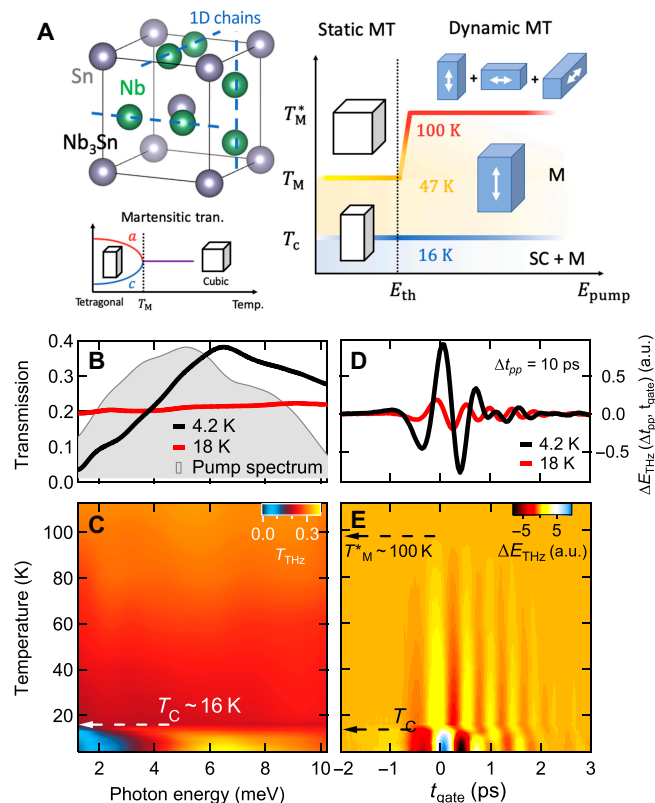


**Fig. 1.** (A) Left: The crystal structure of  $\text{Nb}_3\text{Sn}$  and martensitic transition (MT). Right: Phase diagram. Dynamic MT occurs with  $E_{\text{pump}} > E_{\text{th}}$  and  $T < T_M^*$  at  $T > T_M$ , vibration is equal superposition of the 3 directions, thus the cubic symmetry is intact. (B) Probe transmission rate  $T(\omega)$  shown together with the pump spectra (gray shade). (C) 2D plot of  $T(\omega)$  (without pump). (D) Transmitted probe field change  $\Delta E_{\text{THz}}$  caused by terahertz pumps, where  $\Delta E_{\text{THz}} = E_{\text{Trans}}^{\text{pump}} - E_{\text{Trans}}^{\text{NoPump}}$ . (E) 2D plot of  $\Delta E_{\text{THz}}$  (with terahertz pump). A “kink” occurs at  $T_C \sim 16$  K, and  $\Delta E_{\text{THz}}$  signals vanish at  $T_M^* \sim 100$  K. The terahertz pump electric field strength used is 940 kV/cm. a.u., arbitrary units.

In this letter, we present a light-induced metastable, martensitic phase out of equilibrium in  $\text{Nb}_3\text{Sn}$  obtained by single-cycle terahertz pumping. Above a critical terahertz pump field threshold, the post-quench nonequilibrium state is characterized by a depletion of terahertz spectral weight (SW) due to the splitting of degenerate  $\Gamma_{12}$  band that corresponds to the enhancement of martensitic phase. These terahertz-driven band splitting results are in contrast to optical pump, where we observe a dominant thermal melting of the high energy  $\Gamma_{12}$  gaps with increased terahertz conductivity. The photoinduced nonequilibrium martensitic phase displays the nonthermal electrodynamic that persists up to a critical  $T_M^* \sim 2T_M \sim 100$  K, i.e., doubling of the equilibrium value, for longer than 1 ns. Our theoretical modeling underpins a  $\Gamma_{12}$  phonon tuning mechanism of the martensitic instability and explains, particularly, the enhanced MT, i.e., the doubling of  $T_M$ , and conductivity SW depletion by  $E_u$  phonon-induced changes of  $\Gamma_{12}$  bands and DOS at  $E_F$ .

## Results and Discussion

The sample measured in the experiment is a 20-nm  $\text{Nb}_3\text{Sn}$  film grown on (100)-oriented sapphire single-crystalline substrates by pulsed laser deposition. Single-cycle terahertz pump pulses were generated by a tilted-pulse front phase matching through 1.3% MgO-doped  $\text{LiNbO}_3$  crystal. The peak electric field is as large as 1,000 kV/cm, and the spectrum (gray shade, Fig. 1B) covers  $\sim 1$  to 10 meV. Complex transmission  $\tilde{t}(\omega)$  is obtained by Fourier transformation of transmitted terahertz probe field in time domain. Frequency-dependent optical conductivities  $\sigma_1(\omega)$  and  $\sigma_2(\omega)$  extracted from  $\tilde{t}(\omega)$  measure dissipative and inductive responses, respectively [18,28–32].

Figure 1B presents the static terahertz transmission of  $\text{Nb}_3\text{Sn}$   $T(\omega) = |\tilde{t}(\omega)|$  at 4.2 and 18 K. The quasiparticle excitation gap  $2\Delta_{\text{SC}}$  gives rise to the SC state lineshape (black line), while the normal state spectrum (red line) is largely featureless, tilting slightly up toward higher frequency. A 2-dimensional (2D) false-color plot of terahertz transmission spectra  $T(\omega)$  at various temperatures (Fig. 1C) shows distinctly different shapes below and above the critical temperature  $T_C \sim 16$  K. There, the transmission peak diminishes and redshifts with increasing temperature, as well as completely vanishes when approaching  $T_C$ . Our next focus is the terahertz pumping of martensitic normal states above  $T_C$ . Figure 1C shows that equilibrium transmission spectra above  $T_C$  show very little changes in the measured frequency range, i.e., the static terahertz conductivity is not very sensitive to the martensitic normal state order.

In strong contrast, nonequilibrium signals after terahertz pump centered at  $\sim 5$  meV show a clear temperature dependence in the normal state. Figure 1D shows typical pump-induced changes of transmitted field  $\Delta E_{\text{THz}}$  in time domain at  $\Delta t_{\text{pp}} = 10$  ps. The normal state, 18-K trace shows a clear phase shift and amplitude reduction in comparison with the 4.2-K trace. Figure 1E presents a 2D false plot of  $\Delta E_{\text{THz}}$  of up to  $\sim 110$  K. Again, normal state is well separated from SC state across  $T_C$ . Most intriguingly, clear  $\Delta E_{\text{THz}}$  signals are detected in the normal state and persist up to 100 K, i.e.,  $T_M^* \sim 2T_M$ , indicative of a photoinduced nonequilibrium order far above  $T_M$ .

To further underpin the terahertz pump-induced  $T_M^*$  phase, Fig. 2A shows pump-induced differential transmission  $\Delta E_{\text{THz}}$  under conventional optical pump with 1.55 eV of photon energy. Here, the optically induced terahertz signals (black

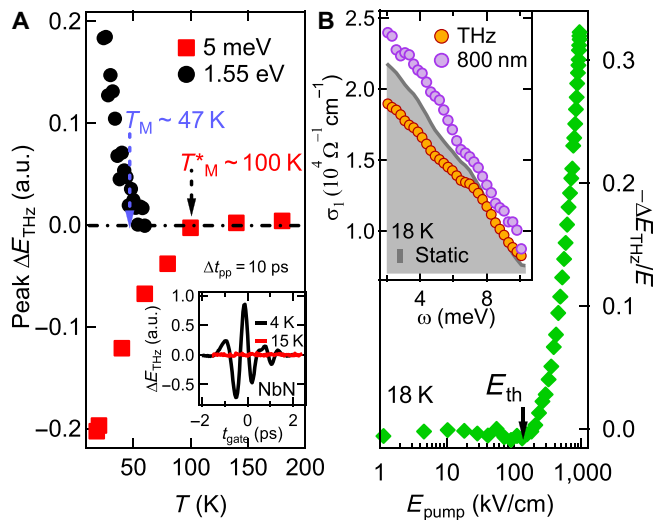


**Fig. 2.** (A) Temperature dependence of pump induced change  $\Delta E_{\text{THz}}$  under terahertz and 1.55-eV photoexcitation. MT temperatures  $T_M$  and  $T_M^*$  for vanishing  $\Delta E_{\text{THz}}$  under optical and terahertz pumps are marked by purple and black arrows, respectively. Inset: No pump-induced change is observed in an NbN superconductor above  $T_c = 14$  K. (B) Pump field dependence of  $\Delta E_{\text{THz}}$  at 18 K shows a threshold  $E_{\text{th}}$  at 130 kV/cm. Inset: Nonequilibrium conductivity  $\sigma_1(\omega)$  under terahertz and 1.55-eV pump compared to the thermal equilibrium state at 18 K.

circles) vanish at the equilibrium transition at  $T_M = 47$  K. These results clearly establish ultrafast optically induced  $\Delta E_{\text{THz}}$  as an effective probe for the equilibrium martensitic order. In contrast, the 5-meV terahertz photoexcitation clearly establishes the nonzero  $\Delta E_{\text{THz}}$  signals up to  $T_M^*$  indicative of “order parameter-like” response for the nonequilibrium martensitic phase.

Further experimental evidence associating the terahertz-driven phase transition is presented in Fig. 2B, which plots terahertz pump field dependence of  $\Delta E_{\text{THz}}$  signals at a fixed time delay  $\Delta t_{\text{pp}} = 10$  ps. It is clearly visible that the signal is negligibly small at terahertz field strengths of less than  $E_{\text{th}} \sim 130$  kV/cm but increases significantly above it. Such distinct threshold behavior of the terahertz-driven dynamics is not limited by our noise floor, which is a hallmark of the nonequilibrium phase transition to an induced martensitic phase. For comparison, no terahertz pump-induced change is observed in a NbN superconductor in the normal state without the martensitic order, e.g., the 15-K trace (red line, inset of Fig. 2A) for NbN versus the 18-K trace (red line, Fig. 1D) for Nb<sub>3</sub>Sn.

The nonequilibrium response function  $\sigma_1(\omega)$  in the inset of Fig. 2B reveals different behaviors for 1.55-eV (optical, purple) and 5-meV (terahertz, orange) pumping, which distinguish thermal versus nonthermal electrodynamics. After high-photon energy, 1.55-eV pump excitation, the low-frequency conductivity gains an additional SW over its equilibrium (no pump) values (gray shade), i.e.,  $\Delta\sigma_1(\omega) > 0$ . This can be understood as melting of the high-energy electronic gaps that develop at the  $T_M$  transition from  $\Gamma_{12}$  phonon condensation (dimerization). The latter leads to SW transfer to the Fermi surface by suppressing the martensitic phase via hot phonons and electrons excited by the high-energy photons. However, the 5-meV pump photon energy is far below the gap and, thus, cannot quench it. Instead, it reverses the SW transfer to high energy by reducing  $\sigma_1(\omega)$ .  $\Delta\sigma_1 < 0$  is fully consistent with the expectation for an enhanced martensitic order, i.e., more states take part in condensation. Because  $5 \text{ meV} < k_B T_M$ , the thermal quench does

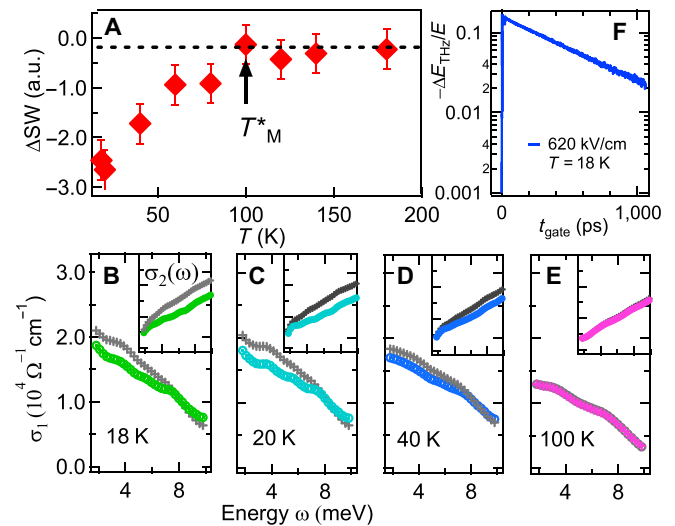


**Fig. 3.** (A) Spectral weight change  $\Delta\text{SW}$  integrated from 2 to 10 meV under the highest driving field of terahertz excitation. (B to E) Real part of conductivity  $\sigma_1(\omega)$  compared to thermal equilibrium at various temperatures with  $\sigma_2(\omega)$  shown in inset. (F)  $\Delta E_{\text{THz}}/E$  temporal dynamics at terahertz pump field of 620 kV/cm and 18 K.

not occur in this case. Note also that the electric field for the optical pump used in Fig. 2B is  $\sim 330$  kV/cm, which is larger than the terahertz pumping field threshold needed to drive the martensitic phase transition. Therefore, the above  $\sigma_1(\omega)$  measurement confirms our interpretation. The suppression and enhancement difference for high- and low-energy pump rationalizes the opposite sign for  $\Delta E_{\text{THz}}$  in Fig. 2A. This is consistent with an elevated transition temperature  $T_M^*$  and, thereby, enhanced the nonequilibrium martensitic order by acquiring an extra SW from the Fermi surface, as quantitatively substantiated later.

Figure 3 presents extensive conductivity spectra measurement and SW analysis in the normal state to investigate martensitic dynamics under intense terahertz radiation. The integrated SW change  $\Delta\text{SW}$  (2 to 10 meV) induced by the terahertz pumping is shown in Fig. 3A at various temperatures in the normal state, together with complex conductivity spectra,  $\sigma_1(\omega)$  and  $\sigma_2(\omega)$ , shown in Fig. 3B to E. The most salient feature is the depleted SW, i.e.,  $\Delta\text{SW} < 0$ , which emerges elusively below  $T_M^*$ . Such SW removal in  $\sigma_1(\omega)$  corresponds to a reduction in  $\sigma_2(\omega)$  (inset) as compared to thermal-equilibrium states (gray crosses, Fig. 3B to E), which is correlated by Kramers–Kronig transformation. Because the total integrated SW is conserved, the missing spectral component is expected to transfer to higher-energy electronic states beyond the measurement energy window, which gives rise to a transient increase of  $T_M$  to  $T_M^*$ . Such experimental evidence indicates strong correlation between terahertz-controlled SW transfer and martensitic order. Furthermore, the  $T_M^*$  phase appears to be metastable, as witnessed by the long  $\sim 1$ -ns relaxation time, e.g., as shown in 620-kV/cm trace (blue line) in Fig. 3F.

Despite different proposals [24–26,33,34], it is generally accepted that MT arises from a mechanism similar as Jahn–Teller effect [23,25], i.e., the instability of lattice distortion is hinged with the lifting of degenerate levels ( $\Gamma_{12}$  electronic bands for Nb<sub>3</sub>Sn). Such a pure lattice–charge interaction (spin-independent) elucidates the situation of its less intertwining with SC [24] and also distinguishes MT from, for instance, nematicity instability in Fe-SC [6], which features an intimate interplay

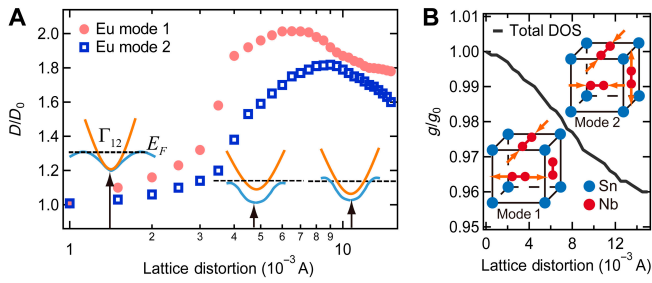


**Fig. 4.** (A) DOS of two equivalent  $\Gamma_{12}$  electronic bands and (B) total DOS  $g$  at Fermi level under finite lattice distortions (compared to its equilibrium  $D_0, g_0$ ). Inset in (A): The schematic of  $\Gamma_{12}$  bands under lattice distortion. Inset in (B): Two  $E_u$  phonon modes are manifested as lattice vibration of Nb atoms in chains along 3 different directions.

with spin [35] and also possibly with SC [36]. Therefore, constructing Landau free energy [24,25] that includes proper lattice–electron coupling should capture the physics regarding  $T_M$  enhancement. To this end, we consider degenerate  $\Gamma_{12}$  electronic bands crossing the FL (inset, Fig. 4A) and strong electron–phonon coupling [24–26,33,37]. Two degenerate  $E_u$  phonon modes involved are shown in Fig. 4B (inset). It has been proposed that the transition temperature  $T_M$  is proportional to the DOS of  $\Gamma_{12}$  electronic bands at the FL [25]. Our physical picture and simulations below demonstrate that  $\Gamma_{12}$  lattice vibration driven by low-energy photoexcitation close to  $E_u$  phonon resonances is able to lift the degeneracy and modify the DOS of the  $\Gamma_{12}$  band, as illustrated in the inset of Fig. 4A. Active modulations of the MT temperature, correlation gap, and electronic order are achieved by intense terahertz radiation, which is absent for high-energy, optical pumping with photon energy far above the  $E_u$  phonon resonances. The  $\Gamma_{12}$  lattice vibration most relevant to the martensitic phase can be understood as dimerization of the Nb atom chain along different axes ( $E_u$  symmetry, inset of Fig. 4B) similar to a charge density wave but confined to a single unit cell with wave vector  $q = 0$ .

To put the abovementioned physical picture on a sound footing, we lay out first-principle simulations of the phonon-assisted tuning of the martensitic phase (see the Supplementary Materials for details). The  $\Gamma_{12}$  phonon contains 2 degenerate modes at  $\Gamma$  point in Brillouin zone (B.Z.), which are (deduced from symmetry),

$$\begin{aligned} Q_1 &= \frac{A_1}{2} (-u_{2x} + u_{1x} + u_{4y} - u_{3y}) \\ Q_2 &= \frac{A_2}{2\sqrt{3}} (2u_{6z} - 2u_{5z} - u_{2x} + u_{1x} - u_{4y} + u_{3y}) \end{aligned} \quad (1)$$

$u_{i\sigma}$  stand for the displacement of  $i$ th Nb atoms in the  $\sigma$  Cartesian component. The  $x$  coordinates in Fig. 4 correspond to  $A_1$  and  $A_2$  in the above equations.

The total free energy can be constructed based on the two  $E_u$  modes,

$$\begin{aligned} F &= \frac{1}{2} V c_0 u^2 + \frac{1}{2} \omega^2 (Q_1^2 + Q_2^2) + \zeta \sqrt{V c_0} \cdot \omega u Q_1 \\ &+ V n \mu - 2k_B T (S_{b1} + S_{b2}) \end{aligned} \quad (2)$$

where  $V$  is unit cell volume,  $c_0$  is force constant,  $\mu$  is chemical potential, and  $u$  is defined by,

$$u = (2e_{zz} - e_{xx} - e_{yy}) / \sqrt{6} \quad (3)$$

where  $e_{xx}$ ,  $e_{yy}$ , and  $e_{zz}$  are the diagonal components of strain tensors.  $S_{b1}$  and  $S_{b2}$  are the entropy due to the 2  $\Gamma_{12}$  electronic bands, which are expressed as,

$$S_{iB} = \sum_k \ln [1 + \exp[-(\varepsilon_k^i - \mu)] / k_B T] \quad (4)$$

The zero-order  $H_0$  of band energies  $\varepsilon_k$  can be simplified as parabolic, which are plausible approximations for dispersion near the  $\Gamma$  point in B.Z. It will be perturbed by the following Hamiltonian  $H_e = H_0 + H'$ ,

$$\begin{aligned} H' &= \left[ \frac{\eta_i \omega}{\sqrt{nV}} Q_2 + \frac{\hbar^2}{2m} \frac{1}{\sqrt{2}} (k_x^2 - k_y^2) \right] (c_1^\dagger c_2 + c_2^\dagger c_1) \\ &+ \left[ \eta_0 \sqrt{\frac{c_0}{n}} u + \frac{\eta_i \omega}{\sqrt{nV}} Q_1 + \frac{\hbar^2}{2m} \frac{1}{\sqrt{6}} (3k_z^2 - k^2) \right] (c_2^\dagger c_2 - c_1^\dagger c_1) \end{aligned} \quad (5)$$

In above, we have ignored the  $k$  index for  $c_1, c_2$ , etc. Note that  $\eta_0$  and  $\eta_i$  come into  $F$  through  $\varepsilon_k^i$ .

In order to account for the MT, the model has included several degrees of freedom: the elastic distortion (tensor)  $u$ , optical phonon modes  $Q_1, Q_2$ , electron entropy, and  $e$ -phonon coupling. Minimize  $F$  with respect to  $u, Q_1, Q_2$ , and  $\mu$ , yielding the equilibrium lattice displacement, which relies on numerical solutions. It shows that the critical  $T_M$  is approximately proportional with a parameter  $\alpha$  in a broad regime, i.e.,  $k_B T_M / \varepsilon_F \propto \alpha$ .

$$\alpha = 2a_0^3 D(\varepsilon_F) G_0^2,$$

$$G_0 = |\eta_0| \sqrt{1 + \frac{(\eta_i - \zeta \eta_0)^2}{(1 - \zeta^2) \eta_0^2}} \quad (6)$$

$D(\varepsilon_F)$  is  $\Gamma_{12}$  DOS at FL, and  $a_0$  is the lattice parameter of the undistorted unit cell (cubic). Notice that  $a_0$  and  $G_0$  could largely be taken as constant, then it yields  $T_M \propto \alpha \propto D(\varepsilon_F)$ . In a dynamic scenario,  $D(\varepsilon_F)$  could be an instantaneous variable [38]. Previous discussion adopted a coarse approximation of constant DOS [25,34]. Here, we seek for an accurate depiction with density functional theory (DFT) and a frozen phonon approximation. [In DFT calculation, the parameters  $Q_i, \phi$  are described by the atom displacements from equilibrium position and unit cell shape (values of  $a$  and  $c$ ), respectively. Frozen phonon means calculating instantaneous electronic structure with a fixed ion configuration]. We will see that lattice distortion further increases  $D(\varepsilon_F)$ , providing positive feedback to MT. Such mutual enhancement alludes to an incarnation of phonon condensation in a semiclassical framework (for  $Q$  is not quantized in this model).

Next, we evaluate the  $\Gamma_{12}$ -DOS change with the presence of  $\Gamma_{12}$  phonon modes  $Q_1, Q_2$ , and  $\phi$  is set zero, i.e.,  $a = c$ . The PAW (projector augmented wave) method [39] and Perdew–Burke–Ernzerhof exchange–correlation functional [40] are employed in DFT calculation. In Fig. 4A,  $\Gamma_{12}$ -DOS at FL is plotted against displacement amplitudes of Nb away from its equilibrium position (thus proportional to  $Q$ ).  $\Gamma_{12}$ -DOS undergoes a sharp

increase above threshold at 0.002 Å and reaches a maximum 2-time enhancement at displacement as small as 0.006 Å, followed by a slight drop under further distortion. The corresponding band movement is shown by insets of Fig. 4A: Initially, 1 of the 2  $\Gamma_{12}$  bands is below FL and starts to cross FL when displacements reach the threshold, and after that, the slight drop is due to the band “slope” change at FL. In contrast, the change of the total DOS is merely  $\sim 4\%$  (Fig. 4B). Mind that dissipation keeps changing displacement amplitudes, and thus, practical observation is an average over a range of amplitudes, which will smooth out the DOS variation. With these realistic factors,  $\Gamma_{12}$ -DOS actually suggests the following: First, there exists a threshold for  $E_{\text{pump}}$  to induce the MT; second, above the threshold, the  $T_M$  is quickly enhanced to  $T_M^* \sim 2T_M$  and then  $T_M^*$  becomes insensitive to  $E_{\text{pump}}$ .

Note that the induced lattice distortion is transcribed to an enhanced  $T_M^*$ . The role of the terahertz excitation is to drive the phonon condensation, which is accounted by the frozen phonon’s amplitudes. This effect comes into play via Eq. 6 and induces MT phase at a higher temperature than the equilibrium one. The exact behaviors of  $Q_1$  and  $Q_2$  as functions of driving field could be complex, which depends on details of both electronic bands and phonon excitations. However, the threshold behavior is clearly correlated and observed in both experiment and theory, as shown in Figs. 2B and 4A, respectively.

Finally, we discuss on how to rationalize the kink at  $T_c$  and why there is no special signature occurring at the original  $T_M = 47$  K in the nonequilibrium data (Fig. 1E). In fact, these salient features are direct consequences of phase continuity. Following the general theoretical framework, we express SC contribution as  $F_{\text{SC}} = c_1 |\psi| + c_2 |\psi|^2 + \dots$  and  $\Delta E_{\text{THz}} = F(\phi) + F_{\text{SC}}(\psi)$ , where  $\psi$  and  $\phi$  are SC order and martensitic order, respectively. The kink is a discontinuity of derivative with temperature. We find (see the Supplementary Materials) at  $T_c$ ,  $\partial_T \Delta E_{\text{THz}} \rightarrow m_1 \phi'$  for  $T > T_c$ , and  $\partial_T \Delta E_{\text{THz}} \rightarrow m_1 \phi' + c_1 |\psi|'$  for  $T < T_c$ . Clearly, there is discontinuity because of  $c_1 |\psi|'$  ( $|\psi|' \neq 0$  as  $T \rightarrow T_c^-$  is required by second-order phase transition). However, there is no discontinuity at  $T_M$ , as  $\partial_T \Delta E_{\text{THz}} \rightarrow m_1 \phi'$  at both sides of  $T_M$ . Mind that the continuous  $\phi'$  is guaranteed by phase continuity, because if  $\phi'$  is discontinuous at  $T_M$ , then there must be another phase transition (based on Ehrenfest classification). In other words, if kink is observed at  $T_M = 47$  K, the signals between  $T_M$  and  $T_M^*$  should interpret as different orders (a new phase might have formed). These facts are consistent with our conclusion of the  $T_M^*$  phase. Moreover, note also that there exhibits no kink feature in the equilibrium data (Fig. 1C). In principle, phase transition should have its signature on thermodynamic measurements. However, MT is a tiny structure distortion with  $a/c$  change of  $\sim 0.9\%$ . The corresponding change in terahertz conductivity is beyond the resolution provided by our static terahertz conductivity measurement. In contrast, dynamic driving allows additional phonon condensation and background-free detection, which amplify the distortion and make the signals more visible.

Terahertz pump pulse is up to  $\sim 10$  meV, which can excite the  $\Gamma_{12}$  resonance nonthermally. In contrast, the high-energy photons (1.55 eV) will significantly heat up the electronic population in the  $\Gamma_{12}$  bands due to the large energy mismatch. Moreover, we note that our calculation is consistent with the most recent DFT (local density approximations) simulation [23]. The accuracy for very small lattice distortion is needed to explain our experimental results.

## Conclusion

In conclusion, we demonstrate a light-enhanced martensitic phase driven by intense, single-cycle terahertz fields, which manifests as a substantially enhanced critical temperature  $T_M^* \sim 2T_M$ . Such a terahertz pump-induced MT can be understood as removal of SWs in the vicinity of the FL. First-principle calculations reveal an effective nonthermal modulation of degenerate  $\Gamma_{12}$  electronic bands that determine the martensitic phase and consistently explain all the key experimental features. Especially, we find that  $D(\varepsilon_F)$  is not enhanced until vibration reaches a threshold amplitude. The theoretical results fully explain our observations, such as the presence of  $E_{\text{th}}$  for  $E_{\text{pump}}$ . Our work provides compelling implications for using  $\text{Nb}_3\text{Sn}$  for quantum technology, e.g., doped  $\text{Nb}_3\text{Sn}$  is still the material of choice to replace Al-based transmon qubits and also supports high-current/magnetic field applications, despite much improved  $T_c$  in unconventional superconductors.

## Acknowledgment

**Funding:** This work was supported by the U.S. Department of Energy, Office of Science, Basic Energy Sciences, Materials Science and Engineering Division under contract no. DEAC02-07CH11358 (scientific drive, THz spectroscopy characterization of Martensitic phase, and theoretical prediction and analysis). Work was also supported by the U.S. DOE, Office of Science, National Quantum Information Science Research Centers, Superconducting Quantum Materials and Systems Center (SQMS), under contract no. DE-AC02-07CH11359 (THz spectroscopy of superconducting phase). Work at the University of Wisconsin was supported by the Department of Energy Office of Basic Energy Sciences under award no. DE-FG02-06ER46327 (structural and electrical characterizations) and Department of Energy grant no. DE-SC100387-020 (sample growth). Theory work at the University of Alabama, Birmingham was supported by the U.S. Department of Energy under contract no. DE-SC0019137 (to I.E.P.). The ultrafast laser used was partially supported by National Science Foundation EECs 1611454. **Competing interests:** The authors declare that they have no competing interests.

## Data Availability

The data that support the plots within this paper and other findings of this study are available from the corresponding author upon reasonable request.

## References

1. Yang X, Vaswani C, Sundahl C, Mootz M, Luo L, Kang JH, Perakis IE, Eom CB, Wang J. Lightwave-driven gapless superconductivity and forbidden quantum beats by terahertz symmetry breaking. *Nat Photonics*. 2019;13:707–713.
2. Fausti D, Tobey RI, Dean N, Kaiser S, Dienst A, Hoffmann MC, Pyon S, Takayama T, Takagi H, Cavalleri A. Light-induced superconductivity in a stripe-ordered cuprate. *Science*. 2011;331(6014):189–191.
3. Luo L, Mootz M, Kang JH, Huang C, Eom K, Lee JW, Vaswani C, Collantes YG, Hellstrom EE, Perakis IE, et al. Quantum coherence tomography of lightwave-controlled superconductivity. *Nat Phys*. 2022; 10.1038/s41567-022-01827-1.

4. Yang X, Luo L, Mootz M, Patz A, Bud'ko SL, Canfield PC, Perakis IE, Wang J. Non-equilibrium pair breaking in  $\text{Ba}(\text{Fe}_{1-x}\text{Co}_x)_2\text{As}_2$  superconductors: Evidence for formation of a photoinduced excitonic state. *Phys Rev Lett*. 2018;121:267001.
5. Mootz M, Luo L, Wang J, Perakis E. Visualization and quantum control of light-accelerated condensates by terahertz multi-dimensional coherent spectroscopy. *Commun Phys*. 2022;5:47.
6. Patz A, Li T, Ran S, Fernandes RM, Schmalian J, Bud'ko SL, Canfield PC, Perakis IE, Wang J. Ultrafast observation of critical nematic fluctuations and giant magnetoelastic coupling in iron pnictides. *Nat Commun*. 2014;5:3229.
7. Li T, Patz A, Mouchliadis L, Yan J, Lograsso TA, Perakis IE, Wang J. Femtosecond switching of magnetism via strongly correlated spin-charge quantum excitations. *Nature*. 2013;496:69–73.
8. Patz A, Li T, Liu X, Furdyna JK, Perakis IE, Wang J. Ultrafast probes of nonequilibrium hole spin relaxation in the ferromagnetic semiconductor  $\text{GaMnAs}$ . *Phys Rev B*. 2015;91:155108.
9. Patz A, Li T, Luo L, Yang X, Bud'ko S, Canfield PC, Perakis IE, Wang J. Critical speeding up of nonequilibrium electronic relaxation near nematic phase transition in unstrained  $\text{Ba}(\text{Fe}_{1-x}\text{Co}_x)_2\text{As}_2$ . *Phys Rev B*. 2017;95:165122.
10. Luo L, Yang X, Liu X, Liu Z, Vaswani C, Cheng D, Mootz M, Zhao X, Yao Y, Wang C-Z. Ultrafast manipulation of topologically enhanced surface transport driven by mid-infrared and terahertz pulses in  $\text{Bi}_2\text{Se}_3$ . *Nat Commun*. 2019;10:607.
11. Sie EJ, Nyby CM, Pemmaraju CD, Park SJ, Shen X, Yang J, Hoffmann MC, Ofori-Okai BK, Li R, Reid AH, et al. An ultrafast symmetry switch in a Weyl semimetal. *Nature*. 2019;565:61–66.
12. Vaswani C, Wang LL, Mudiyansele DH, Li Q, Lozano PM, Gu GD, Cheng D, Song B, Luo L, Kim RHJ, et al. Light-driven raman coherence as a nonthermal route to ultrafast topology switching in a Dirac semimetal. *Phys Rev X*. 2020;10:021013.
13. Yang X, Vaswani C, Sundahl C, Mootz M, Gagel P, Luo L, Kang JH, Orth PP, Perakis IE, Eom CB, et al. Terahertz-light quantum tuning of a metastable emergent phase hidden by superconductivity. *Nat Mater*. 2018;17:586–591.
14. Li X, Qiu T, Zhang J, Baldini E, Lu J, Rappe AM, Nelson KA. Terahertz field-induced ferroelectricity in quantum paraelectric  $\text{SrTiO}_3$ . *Science*. 2019;364:1079–1082.
15. Aoki H, Tsuji N, Eckstein M, Kollar M, Oka T, Werner P. Nonequilibrium dynamical mean-field theory and its applications. *Rev Mod Phys*. 2014;86:779–837.
16. Fradkin E, Kivelson SA, Tranquada JM. Colloquium: Theory of intertwined orders in high temperature superconductors. *Rev Mod Phys*. 2015;87:457–482.
17. Vaswani C, Mootz M, Sundahl C, Mudiyansele DH, Kang JH, Yang X, Cheng D, Huang C, RHJ K, Liu Z, et al. Terahertz second-harmonic generation from lightwave acceleration of symmetry-breaking nonlinear supercurrents. *Phys Rev Lett*. 2020;124:207003.
18. Liu Z, Vaswani C, Yang X, Zhao X, Yao Y, Song Z, Cheng D, Shi Y, Luo L, Mudiyansele D-H, et al. Ultrafast control of excitonic Rashba fine structure by phonon coherence in the metal halide perovskite  $\text{CH}_3\text{NH}_3\text{PbI}_3$ . *Phys Rev Lett*. 2020;124:157401.
19. Dienst A, Hoffmann MC, Fausti D, Petersen JC, Pyon S, Takayama T, Takagi H, Cavalleri A. Bi-directional ultrafast electric-field gating of interlayer charge transport in a cuprate superconductor. *Nat Photonics*. 2011;5:485–488.
20. Yang X, Zhao X, Vaswani C, Sundahl C, Song B, Yao Y, Cheng D, Liu Z, Orth PP, Mootz M, et al. Ultrafast nonthermal terahertz electrodynamics and possible quantum energy transfer in the  $\text{Nb}_3\text{Sn}$  superconductor. *Phys Rev B*. 2018;99:094504.
21. Kozina M, Fechner M, Marsik P, van Driel T, Glowina JM, Bernhard C, Radovic M, Zhu D, Bonetti S, Staub U, et al. Terahertz-driven phonon upconversion in  $\text{SrTiO}_3$ . *Nat Phys*. 2019;15:387–392.
22. Yang X, Luo L, Vaswani C, Zhao X, Yao Y, Cheng D, Liu Z, Kim RHJ, Liu X, Dobrowolska-Furdyna M, et al. Light control of surface-bulk coupling by terahertz vibrational coherence in a topological insulator. *NPJ Quantum Mater*. 2020;5:13.
23. Sadigh B, Ozoliņš V. Structural instability and electronic excitations in  $\text{Nb}_3\text{Sn}$ . *Phys Rev B*. 1998;57:2793–2800.
24. Bilbro G, McMillan WL. Theoretical model of superconductivity and the martensitic transformation in A15 compounds. *Phys Rev B*. 1976;14:1887–1892.
25. Kataoka M. Theory of the structural phase transition in A15 compounds. *Phys Rev B*. 1983;28:2800–2815.
26. Bhatt RN, McMillan WL. Landau theory of the martensitic transition in A-15 compounds. *Phys Rev B*. 1976;14:1007–1027.
27. Batterman BW, Barrett CS. Low-temperature structural transformation in  $\text{V}_3\text{Si}$ . *Phys Rev*. 1966;145:296–301.
28. Luo L, Chatzakis I, Wang J, Niesler FB, Wegener M, Koschny T, Soukoulis CM. Broadband terahertz generation from metamaterials. *Nat Commun*. 2014;5:3055.
29. Luo L, Men L, Liu Z, Mudryk Y, Zhao X, Yao Y, Park JM, Shinar R, Shinar J, Ho K-M, et al. Ultrafast terahertz snapshots of excitonic Rydberg states and electronic coherence in an organometal halide perovskite. *Nat Commun*. 2017;8:15565.
30. Wang J, Graham MW, Ma Y, Fleming GR, Kaundl RA. Ultrafast spectroscopy of midinfrared internal exciton transitions in separated single-walled carbon nanotubes. *Phys Rev Lett*. 2010;104:177401.
31. Luo L, Chatzakis I, Patz A, Wang J. Ultrafast terahertz probes of interacting dark excitons in chirality-specific semiconducting single-walled carbon nanotubes. *Phys Rev Lett*. 2015;114:107402.
32. Luo L, Liu Z, Yang X, Vaswani C, Cheng D, Park J-M, Wang J. Anomalous variations of spectral linewidth in internal excitonic quantum transitions of ultrafast resonantly excited single-walled carbon nanotubes. *Phys Rev Mater*. 2019;3:026003.
33. Bhatt RN. Microscopic theory of the martensitic transition in A-15 compounds based on a three-dimensional band structure. *Phys Rev B*. 1977;16:1915–1932.
34. Noolandi J, Sham LJ. Theory of structural phase transition in  $\text{Nb}_3\text{Sn}$ . *Phys Rev B*. 1973;8:2468–2475.
35. Glasbrenner JK, Mazin II, Jeschke HO, Hirschfeld PJ, Fernandes RM, Valenti R. Effect of magnetic frustration on nematicity and superconductivity in iron chalcogenides. *Nat Phys*. 2015;11:953–958.
36. Lederer S, Schattner Y, Berg E, Kivelson SA. Enhancement of superconductivity near a nematic quantum critical point. *Phys Rev Lett*. 2015;114:097001.
37. Gor'kov LP. Theory of the properties of superconductors with a  $\beta$ -W structure. *Zh Eksp Teor Fiz*. 1973;65(4):1658–1676.
38. Freericks JK, Liu AY, Quandt A, Geerk J. Nonconstant electronic density of states tunneling inversion for A15 superconductors:  $\text{Nb}_3\text{Sn}$ . *Phys Rev B*. 2002;65:224510.
39. Blöchl PE. Projector augmented-wave method. *Phys Rev B*. 1994;50:17953.
40. Mattheiss LF, Weber W. Electronic structure of cubic  $\text{V}_3\text{Si}$  and  $\text{Nb}_3\text{Sn}$ . *Phys Rev B*. 1982;25:2248–2269.